Effective slip in pressure-driven Stokes flow

By ERIC LAUGA AND HOWARD A. STONE

Division of Engineering and Applied Sciences, Harvard University,
Pierce Hall, 29 Oxford Street, Cambridge, MA 02138, USA

Nano-bubbles have recently been observed experimentally on smooth hydrophobic surfaces; cracks on a surface can likewise be the site of bubbles when partially wetting fluids are used. Because these bubbles may provide a zero shear stress boundary condition and modify considerably the friction generated by the solid boundary, it is of interest to quantify their influence on pressure-driven flow, with particular attention given to small geometries. We investigate two simple configurations of steady pressure-driven Stokes flow in a circular pipe whose surface contains periodically distributed regions of zero surface shear stress. In the spirit of experimental studies probing slip at solid surfaces, the effective slip length of the resulting flow is evaluated as a function of the degrees of freedom describing the surface heterogeneities, namely the relative width of the no-slip and no-shear stress regions and their distribution along the pipe. Comparison of the model with experimental studies of pressure-driven flow in capillaries and microchannels reporting slip is made and a possible interpretation of the experimental results is offered which is consistent with a large number of distributed slip domains such as nano-size and micron-size nearly flat bubbles coating the solid surface. Further, the possibility is suggested of a shear-dependent effective slip length, and an explanation is proposed for the seemingly paradoxical behaviour of the measured slip length increasing with system size, which is consistent with experimental results to date.

1. Introduction

The ability to design, fabricate, pattern and optically probe mechanical structures with micrometre and nanometre length scales has led to many recent studies of liquid motion adjacent to smooth surfaces, e.g. experiments (Pit, Hervert & Léger 2000; Baudry & Charlaix 2001; Zhu & Granick 2001; Bonaccurso, Kappl & Butt 2002; Cheng & Giordano 2002; Craig, Neto & Williams 2001; Raviv *et al.* 2002; Tretheway & Meinhart 2002; Zhu & Granick 2002; Cottin-Bizonne *et al.* 2002) and molecular dynamics simulations (Robbins 1990; Thompson & Troian 1997; Barrat & Bocquet 1999; Cieplak, Koplik & Banavar 2001). The principal question addressed by these investigations concerns the applicability of the no-slip condition at a solid–liquid boundary. In particular, when the fluid does not completely wet an atomically smooth substrate (i.e. non-wetting or partial wetting situations, so-called solvophobic or hydrophobic conditions), then we might expect, or at least it has been conjectured, that the flow may exhibit some manifestations of microscopic slip.

Because any surface treatment to promote slip may have defects where the boundary condition is instead the usual no-slip condition, we were motivated to consider special patterns of slip/no-slip regions where analytical calculations are possible. Such configurations of slip and no-slip domains are also models for regions of

reduced surface stress such as small bubbles attached to solid surfaces as discussed further below. Here, we address the question of pressure-driven flow in a circular pipe that is patterned with alternating regions of no-slip and perfect slip boundary conditions. Such elementary models contain important characteristics features (the slip and no-slip lengths scales) yet allow for simple calculations and some comparisons with experiments can be made.

There have been a few studies of pressure-driven liquid flow in channels or capillaries that exhibit results consistent with slip at the solid boundary; a review of some aspects of this field has been given by Vinogradova (1999). Reports of slip, generally in experiments with partially wetting fluids, have increased in recent years and appear to be in contradiction with older studies which verified convincingly, apparently always in complete wetting conditions, the validity of the no-slip boundary condition (Bean 1972; Quinn *et al.* 1972; Idol & Anderson 1986; Knudstrup, Bitsanis & Westermann-Clark 1995).

In most of the experiments probing slip, a slip length is or can be inferred from measurements. A common definition of a (local) slip length λ at a rigid boundary, with unit normal $\boldsymbol{n}$ directed into the fluid, linearly relates the velocity at the wall to the wall shear strain rate

$$\boldsymbol{u} = \lambda \boldsymbol{n} \cdot ((\nabla \boldsymbol{u}) + (\nabla \boldsymbol{u})^T), \tag{1.1}$$

where λ is assumed to be a material parameter; note that it would also be reasonable to think in terms of a relation between slip velocity and the wall shear stress. This relation was first proposed by Navier (1823) for liquids and was also rigorously derived by Maxwell (1879) in the case of gases, with a slip length of the order of the mean free path of the gas molecules. Alternative models for the velocity–rate-of-strain relationship at a fluid–solid boundary have also been proposed (see e.g. Thompson & Troian 1997). Physically, the slip length is the local equivalent distance below the solid surface at which the no-slip boundary condition would be satisfied if the flow field were extended linearly outside of the physical domain.

The first systematic experimental study reporting slip was apparently reported by Schnell (1956) who measured the flow rate of water in glass capillaries of radius of the order $100\,\mu\mathrm{m}$. When the capillaries were treated with dimethyldichlorosilane to make them hydrophobic, larger flow rates were obtained and they were interpreted as a sign of slip at the wall. The slip length consistent with the results from Schnell (1956), inferred from the pressure drop versus flow rate measurements using equation (2.8) below, can be evaluated to be of the order of $5\,\mu\mathrm{m}$. Churaev, Sobolev & Somov (1984) performed similar measurements for the flow of water in hydrophobic glass capillaries and mercury in untreated glass capillaries of radius of the order of $1\,\mu\mathrm{m}$. In the case of water, results in agreement with the no-slip boundary condition were obtained for low surface hydrophobicity (contact angle smaller than $70°$) but for high surface hydrophobicity larger flow rates were obtained, consistent with slip lengths of about $30\,\mathrm{nm}$. In the case of mercury, with an advancing contact angle of $133°$, results consistent with slip lengths of about $70\,\mathrm{nm}$ were obtained.

More recent investigations were reported by Watanabe, Udagawa & Udagawa (1999) for the flow of aqueous solutions of glycerine through acrylic resin pipes with radii of the order of a centimetre. When the walls of the pipe were treated to be hydrophobic by silica surface coatings, larger flow rates were obtained which were consistent with (very large) slip lengths of approximately $500\,\mu\mathrm{m}$. In these experiments, the contact angle was about $150°$, the surface roughness was about 10 to $100\,\mu\mathrm{m}$, and visible elongated cracks were present on the surface. Further, the observed drag

reduction and also the inferred slip length were found to increase with the viscosity of the solution and, perhaps surprisingly, with an increase in the radius of the pipe.

A physical picture that can be suggested (and was hinted at by Watanabe *et al.* 1999) is that the pipe surface may have air pockets trapped in the cracks along the boundary, with these air pockets acting like a zero shear stress boundary condition; the recently developed super-hydrophobic fractal surfaces contain similar features (Onda *et al.* 1996). A variant of this picture may be applicable even when the surface is smooth, as evidenced by the experimental observation of nano-bubbles on hydrophobic surfaces (Ishida *et al.* 2000; Tyrrell & Attard 2001, 2002). Similar ideas were proposed by Boehnke *et al.* (1999) as an interpretation for the measurement of anomalously high sedimentation velocities of micron-sized spheres with solvophobic surfaces in polar liquids.

Tretheway & Meinhart (2002) used micro particle image velocimetry to measure velocities for the flow of water in rectangular glass microchannels; the measurements included data within 450 nm of the channel surface. When the walls of the channels were treated to be hydrophobic by a nanometre thick coating of OTS (contact angle of 120°, surface roughness of about 2 Å) velocity fields with slip at the wall were reported, consistent with a slip length of about 1 μm. Cheng & Giordano (2002) reported flow rate versus pressure drop measurements for the flow of water and various oils (hexane, tetradecane and silicone oil) in rectangular glass channels of width of about 10 μm and various heights on the scale of tens to hundreds of nanometres. The results for water were always consistent with the no-slip boundary condition but those for the oils showed increased flow rates, consistent with effective slip lengths of order about 10 nm when the height of the channel was chosen smaller than approximately 200 nm; the slip length was also seen to increase systematically with the molecular weight of the oils, and therefore with their viscosity.

Another class of experiments probing flow in nanometre scale gaps uses squeeze flow between atomically smooth surfaces. Experiments exhibiting significant slip, usually shear-dependent, have been reported (Baudry & Charlaix 2001; Craig *et al.* 2001; Zhu & Granick 2001; Bonaccurso *et al.* 2002). We note that results with much smaller slip lengths in these geometries, possibly zero, have also been reported (Chan & Horn 1985; Raviv *et al.* 2002).

Most of the experiments summarized above deduce a slip length from macroscopic flow rate versus pressure drop measurements and we prefer to refer to such slip lengths as either 'macroscopic' or 'effective', which we will denote λ_{eff}. Since we attempt in this paper to make quantitative comparisons with and between different experiments reported in the literature, we therefore distinguish an effective macroscopically deduced slip length λ_{eff} from theories elaborating more microscopic deductions of a local slip (i.e. equation (1.1)) based upon, for example, molecular-dynamics-like approaches. In the latter cases, molecular-scale phenomena are modelled to arrive at a slip condition which is then used in, or proposed as, a macroscopic boundary condition for the Navier–Stokes equations (e.g. see Koplik & Banavar 1995; Denniston & Robbins 2001 and see also the criticism and discussion in Ganesan & Brenner 1999; Koplik & Banavar 1999; Brenner & Ganesan 2000). The slip boundary condition, equation (1.1), is then to be applied at all points on the boundary of a flow configuration.

As a difference, we wish to draw attention in the present paper to the role of surface heterogeneities (and no violation of the no-slip condition between liquids and solids or gas) as a possible explanation for the measured effective slip. The models described in our paper assumes *a priori* that the boundary is heterogeneous in that

	S 1956	CSS 1984	WUU 1999	TM 2002	CG 2002
Liquids used	Water	Water Mercury	Water + glycerin	Water	Water Tetradecane Hexane Silicone oil
Type of surface	Glass	Quartz	Acrylic resin	Glass	Glass
Surface treatment	$(CH_3)_2SiCl_2$	$(CH_3)_3SiCl$	Hydrophobic silica	$CH_3(CH_2)_{17}SiCl_3$	–
Contact angle	–	$70°$–$110°$	$150°$	$120°$	–
Surface roughness	–	–	10–$100\,\mu m$	2–$3\,\text{Å}$	$5\,\text{Å}$
System size R	250–$800\,\mu m$	0.3–$7\,\mu m$	6–$12\,mm$	$30\,\mu m$	40–$200\,nm$
Shear rate $\dot{\gamma}$	100–$3000\,s^{-1*}$	1–$10\,000\,s^{-1*}$	25–$100\,s^{-1*}$	$200\,s^{-1*}$	300–$5000\,s^{-1*}$
Slip length λ_{eff}	2–$8\,\mu m^*$	20–$90\,nm$	200–$450\,\mu m^*$	$1\,\mu m$	10–$30\,nm$
Slip velocity	0.3–$25\,mm\,s^{-1*}$	0.02–$500\,\mu m\,s^{-1*}$	$1\,cm\,s^{-1*}$	$200\,\mu m\,s^{-1*}$	3–$150\,\mu m\,s^{-1*}$
Ratio λ_{eff}/R	0.01	0.005–0.1	0.03	0.03	0.08–0.2
Slip percentage δ_λ	0.97	0.965–0.97	0.97	0.97	0.97
Periodicity L_λ	0.01	0.005–0.01	0.03	0.03	0.08–0.2
Slip size h	2.7–$8.5\,\mu m$	34–$175\,nm$	180–$360\,\mu m$	$902\,nm$	10–$28\,nm$
Distance H	2.8–$8.8\,\mu m$	35–$180\,nm$	190–$370\,\mu m$	$930\,nm$	10–$29\,nm$

TABLE 1. Summary of the parameters and results from the pressure-driven flow experiments of Schnell (1956) (S 1956), Churaev *et al.* (1984) (CSS 1984), Watanabe *et al.* (1999) (WUU 1999), Tretheway & Meinhart (2002) (TM 2002) and Cheng & Giordano (2002) (CG 2002); * results not directly reported but inferred from other experimental results. The last four lines display the results of our model: the values of the slip percentage δ_λ and the dimensionless periodicity L_λ that give the same dimensionless slip length for both the longitudinal and transverse no-shear patterning models (see figure 2), and the resulting dimensional values for the size of the slip regions h and their separation H.

regions of perfect slip ($\lambda = \infty$) exist along an otherwise no-slip ($\lambda = 0$) surface. An effective slip length $\lambda_{eff} \neq 0$ is then calculated using the same style of macroscopic 'measurement' as reported in most experiments.

Another issue that concerns microscopic and macroscopic boundary conditions is the role of surface roughness. As shown by Richardson (1973) using continuum arguments, a small amount of roughness can effectively produce a no-slip boundary condition for the bulk equations, on length scales large compared to the surface roughness, even if the detailed boundary condition is perfect slip on the scale of the roughness (see also Jansons 1988). Robbins (1990) presents related ideas, but from the perspective of molecular dynamics.

In order to understand similarities and differences between the experiments reporting slip in capillaries or microchannels, we give many of their qualitative and quantitative features in table 1; note that many of the entries in table 1 refer to details of the discussion given in §3. Using our macroscopic model of a heterogeneous slip/no-slip surface, and with reference to experimental observations of nano-bubbles by Ishida *et al.* (2000) and Tyrrell & Attard (2001, 2002), we find quantitative results consistent with an interpretation of the various experiments described above where a large number of nano-size and micron-size slip domains cover the solid surface; the suggested physical picture is therefore that of surface heterogeneities producing a macroscopic effective slip. In addition, we suggest the possibility of a shear-dependent effective slip length and finally, based on our model, we offer an interpretation of the apparently paradoxical increase in the effective slip length with system size that has been reported by Watanabe *et al.* (1999) and that is also evident when results from different groups are examined (see table 1).
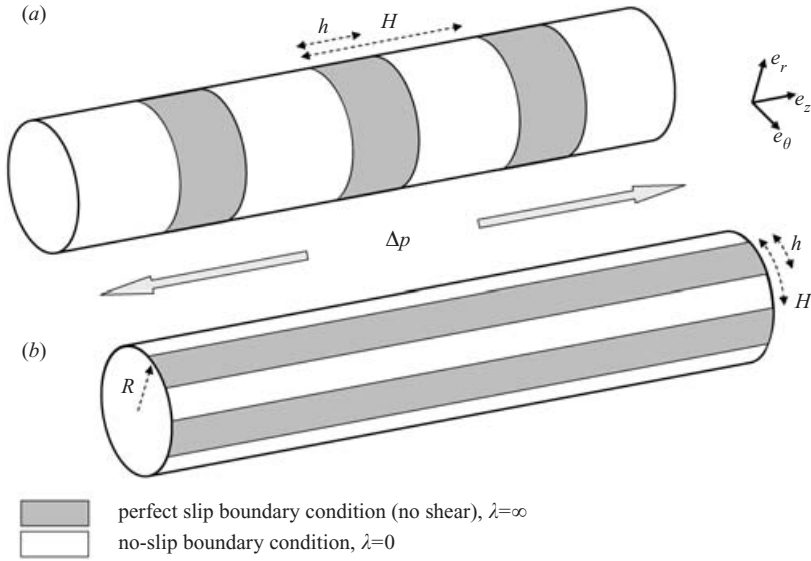
FIGURE 1. Schematic views of the elementary models used: pressure-driven flow in a pipe of radius R with distribution of no-shear regions of width h and separation H; λ denotes the microscopic slip length. (a) The no-shear regions are transverse to the flow direction. (b) The no-shear regions are parallel to the flow direction.

The paper is organized as follows. The two elementary models considered are presented in §2. One is solved in detail in Appendix A and the solution of the second one, from Philip (1972a), is recalled in Appendix B; comparison between these two models is also presented in §2. Because the model of surface heterogeneity motivates several questions for interpreting experimental data, the results for the obtained effective slip lengths are discussed in §3, and comparison is made with and between different experimental results. Finally, we summarize our results in §4.

2. Model and effective slip

2.1. *The two configurations of surface heterogeneity*

We consider in this section two elementary configurations as illustrated in figure 1, namely steady pressure-driven Stokes flow in a pipe of radius R where distributed regions of zero surface stress of width h and separation H are present on the otherwise no-slip surface of the pipe. These configurations are idealized yet they contain the essential features that are needed for a simple model of the consequences of surface heterogeneities on the effective properties of the flow: the length scale of surface heterogeneities and the surface coverage. Note that the perfect slip regions (local infinite slip lengths) are models for the typically small resistance to fluid motion offered by a nearly planar gas–liquid interface.

2.1.1. *Transverse configuration*

In the first configuration (figure 1a) the slip regions are distributed transverse to the flow direction. They take the form of rings of width h transverse to the flow direction and are distributed periodically along the pipe with a period H. The constant axial mean pressure drop is denoted $G = \Delta p/H$, with $\Delta p > 0$ and we investigate this flow in the limit of low Reynolds number, $\rho G R^3/\mu^2 \ll 1$. With this geometry and under

the low-Reynolds-number assumption, the flow equations are those of incompressible Stokes flow in a circular pipe $\mu \nabla^2 \boldsymbol{u} = \nabla p$ and $\nabla \cdot \boldsymbol{u} = 0$, together with the required periodicity of length H. The boundary condition on the no-slip part of the domain is

$$\boldsymbol{u} = \boldsymbol{0} \quad \text{for } r = R, \quad \tfrac{1}{2}h < |z| \leqslant \tfrac{1}{2}H, \quad 0 \leqslant \theta < 2\pi. \tag{2.1}$$

The boundary condition of 'perfect slip' on the other part of the domain is

$$\boldsymbol{t} \cdot \boldsymbol{\sigma} \cdot \boldsymbol{n} = 0 \quad \text{for } r = R, \quad |z| < \tfrac{1}{2}h, \quad 0 \leqslant \theta < 2\pi, \tag{2.2}$$

where $\boldsymbol{\sigma}$ is the stress tensor, and $\boldsymbol{n}$ and $\boldsymbol{t}$ are, respectively, the unit normal and tangent vectors to the surface. Together with the kinematic boundary condition at the surface of the pipe, the boundary conditions can therefore be written as

$$u_r = 0, \quad \sigma_{rz} = \sigma_{r\theta} = 0 \quad \text{for } r = R, \quad |z| \leqslant \tfrac{1}{2}h, \quad 0 \leqslant \theta < 2\pi. \tag{2.3}$$

We non-dimensionalize the above equations and boundary conditions scaling distances by R and velocities by $(GR^2)/\mu$. Below, we use all variables as above except from now on they are dimensionless. Introducing the dimensionless lengths $\ell = h/R$ and $L = H/R$, the flow has now a spatial dimensionless periodicity of L and satisfies the dimensionless Stokes and continuity equations

$$\nabla^2 \boldsymbol{u} = \nabla p, \quad \nabla \cdot \boldsymbol{u} = 0, \tag{2.4}$$

with the boundary conditions

$$\boldsymbol{u} = \boldsymbol{0} \quad \text{for } r = 1, \quad \tfrac{1}{2}\ell < |z| \leqslant \tfrac{1}{2}L, \quad 0 \leqslant \theta < 2\pi, \tag{2.5a}$$

$$u_r = 0, \quad \sigma_{rz} = \sigma_{r\theta} = 0 \quad \text{for } r = 1, \quad |z| \leqslant \tfrac{1}{2}\ell, \quad 0 \leqslant \theta < 2\pi. \tag{2.5b}$$

The solution of (2.4)–(2.5) is accomplished by separation of variables and the solution of dual series equations, and is presented in Appendix A. The azimuthal component of the vorticity is derived in equation (A 6); this leads to an equation for the streamfunction (A 12) which has unknown degrees of freedom that can be found by applying the mixed boundary conditions on the slip/no-slip regions (A 13). The final result for the streamfunction (and therefore both the pressure and velocity fields) is an infinite Fourier series with coefficients satisfying a dual series equation (A 18); such an equation is not in standard form and has to be solved numerically.

2.1.2. *Longitudinal configuration*

In the second configuration (figure 1*b*) the slip regions are distributed parallel to the flow direction. They take the form of infinite stripes of width h parallel to the flow direction and are distributed periodically across the pipe with a period H. The solution to this problem was derived by conformal mapping in Philip (1972*a*) and is recalled in Appendix B.

2.2. *Effective slip length*

For the slip/no-slip patterning displayed in figure 1, we want to evaluate the effective slip length of the flow. In the case of a parallel uniaxial flow in a pipe of radius R satisfying the slip equation (1.1) everywhere on the pipe wall $r = R$ with a slip length λ, the solution for the dimensionless velocity profile is

$$u(r) = \frac{1}{4}(1 - r^2) + \frac{1}{2}\frac{\lambda}{R}. \tag{2.6}$$

The dimensionless total flow rate Q is therefore equal to the Poiseuille flow rate $\pi/8$ augmented by a flow rate due to slip at the wall

$$Q = \frac{\pi}{8}\left(1 + \frac{4\lambda}{R}\right). \tag{2.7}$$

For a general flow with mixed slip/no-slip boundary conditions such as the configurations shwon in figure 1, we define the 'effective slip' length as the slip length of the parallel flow which satisfies (1.1) and (i) is driven by the same pressure gradient and (ii) has the same flow rate as the flow of interest. The effective slip length λ_{eff} is therefore related to the increase in flow rate given by (2.7) and is defined by

$$\frac{\lambda_{eff}}{R} = \frac{1}{4}\left(\frac{8Q}{\pi} - 1\right), \tag{2.8}$$

where Q is the total dimensionless flow rate. Equation (2.8) is effectively how experimental data on pressure drop versus flow rate is converted to a slip length.

By dimensional analysis, and for both configurations shown in figure 1, the dimensional slip length λ_{eff} can be expressed as $\lambda_{eff} = R f(\delta, L)$, where $L = H/R$ is the dimensionless distance between the slip domains and $\delta = h/H$ the percentage of the surface that is perfect slip. When the slip domains are distributed in a longitudinal fashion along the pipe, an exact solution for the effective slip length, denoted $\lambda_{eff,\parallel}$, can be derived from the analytical solutions of Philip (1972a, b) (see also Appendix B). It is given by

$$\frac{\lambda_{eff,\parallel}}{R} = \frac{L}{\pi}\ln\left(\sec\left(\delta\frac{\pi}{2}\right)\right), \tag{2.9}$$

which is valid for all δ and $L < 2\pi$.

When the slip domains are transverse to the flow direction, the effective slip length, denoted $\lambda_{eff,\perp}$, has to be calculated numerically by solving the dual series equation (A 18) and the details are described in Appendix A, §§A.2 and A.3. Because no general analytical solution is available, it is enlightening to determine the asymptotic behaviours for the slip length as a function of δ and L in different regions of the parameter space. This is achieved in Appendix A §A.4 and we find four distinct asymptotic limits:

$$\frac{\lambda_{eff,\perp}}{R} \sim \frac{\delta}{4} \qquad\qquad \text{when } \delta \to 0 \text{ and } L \text{ fixed}, \tag{2.10a}$$

$$\frac{\lambda_{eff,\perp}}{R} \sim \frac{1}{4(1-\delta)} \qquad \text{when } \delta \to 1 \text{ and } L \text{ fixed}, \tag{2.10b}$$

$$\frac{\lambda_{eff,\perp}}{R} \sim \frac{L}{2\pi}\ln\left(\sec\left(\delta\frac{\pi}{2}\right)\right) \quad \text{when } L \to 0 \text{ and } \delta \text{ fixed}, \tag{2.10c}$$

$$\frac{\lambda_{eff,\perp}}{R} \sim \frac{\delta}{4(1-\delta)} \qquad \text{when } L \to +\infty \text{ and } \delta \text{ fixed}. \tag{2.10d}$$

2.3. *Comparison between longitudinal and transverse slip regions*

In the longitudinal case, equation (2.9) leads to asymptotic behaviours for large and small δ, with L fixed, of the form

$$\frac{\lambda_{eff,\parallel}}{R} \sim \frac{L\pi}{4}\delta^2 \qquad\qquad \text{as} \quad \delta \to 0, \tag{2.11a}$$

$$\frac{\lambda_{eff,\parallel}}{R} \sim -\frac{L}{\pi}\ln(1-\delta) \quad \text{as} \quad \delta \to 1. \tag{2.11b}$$

When the percentage of slip is small, the effective slip length decreases more quickly to zero in the case of longitudinal slip slots (equation (2.11*a*), quadratic dependence on δ) than in the case of slip rings (equation (2.10*a*), linear dependence on δ). Consequently, a small amount of slip leads to a much more significant additional flow rate in the case of transverse patterns than in the case of longitudinal patterns. Furthermore, when the percentage of slip is large, the slip length in the case of longitudinal slip slots diverges much more slowly to infinity (equation (2.11*b*), logarithmic divergence) than in the case of transverse regions (equation (2.10*b*), algebraic divergence). Consequently, a small density of no-slip defects on the otherwise no-shear surface of a pipe has a much more significant impact on the friction caused by the pipe when the defects are aligned with the flow direction (the effective slip length is only logarithmically large) than when perpendicular to it.

Note also that the obtained formula, (2.9), is exactly twice that given by equation (2.10*c*); in the limit of small separation between slip regions, longitudinal slip regions result in an effective slip length $\lambda_{eff,\parallel}$ which is exactly twice the slip length $\lambda_{eff,\perp}$ obtained when the slip regions are distributed in a transverse direction to the flow, i.e. $\lambda_{eff,\parallel} = 2\lambda_{eff,\perp}$. The factor of 2 can be interpreted in the following fashion. As a consequence of the spatial structure of the Stokeslet, the fundamental flow field due to a point force, an elongated body sedimenting due to its own weight falls twice as fast if it is oriented vertically than if it is oriented horizontally; said differently, for a given velocity of the body in the fluid, an elongated body exerts twice as much force on the fluid when it is aligned perpendicularly to its direction of motion than when it is aligned parallel to it. As a consequence, for a given wall slip velocity and in the case of small L where the slip regions are approximately two-dimensional, the shear in the longitudinal case will be twice as large as the shear in the transverse case, and therefore the slip length in the parallel case is expected to be twice that in the perpendicular case, i.e. $\lambda_{eff,\parallel} = 2\lambda_{eff,\perp}$.

3. Discussion of experimental results

In light of the two configurations introduced in §2, we analyse here the different experiments described in §1: flow in capillaries (Schnell 1956; Churaev *et al.* 1984; Watanabe *et al.* 1999) and flow in rectangular micro and nanochannels (Cheng & Giordano 2002; Tretheway & Meinhart 2002). These experiments motivate a general discussion of ideas related to slip in §3.1 and we then use in §3.2 the models from §2 to offer a possible quantitative interpretation of experimental results. Finally, we address the possibility of shear-dependent slip lengths in §3.3 and we propose in §3.4 an explanation for the reported increase of effective slip lengths with system size.

The orders of magnitude of the experimental parameters and results obtained by each group, either directly reported or inferred from their papers, are displayed in table 1; in particular, we refer to the slip length reported as an effective value since it is either based upon flow rate versus pressure drop considerations (four out of the five papers) or velocity measurements cross-correlated and averaged in space (Tretheway & Meinhart 2002). The variability of the parameters and corresponding results have to be noted: large variations in the typical system size (more than 5 orders of magnitude in pipe radius or channel width), typical shear strain rates (4 orders of magnitude), typical values for the wall slip velocity (almost 6 orders of magnitude), and effective slip lengths (more than 4 orders of magnitude). However, the variation in the dimensionless slip length λ_{eff}/R, where R is the characteristic channel dimension, is seen to be small; there is only a ratio of 40 between its maximum and minimum

values. Furthermore, the dimensional effective slip length increases systematically with system size from one experiment to the other. This result is also evident in the results reported by Watanabe *et al.* (1999).

3.1. *Comments on the correction to no-slip measurements*

With regard to experimental evidence of slip, we first note that for a given effective slip length λ_{eff}, a set of experimental measurements (whether direct velocity measurements or indirect measurements through determination of friction factors) will only be able to significantly capture the magnitude of the slip if the correction of the flow due to the slip at the wall is much larger than the typical experimental error. If a typical experimental error on pressure, flow rate or velocity measurement is, say, about 1%, the influence of the slip at the wall will only be deducable with confidence from such measurements if the magnitude of the modified flow rate is at least, say to fix ideas, 2% of its no-slip value (note that this is a conservative estimate as experimental errors can sometimes be much larger, such as the 15% uncertainty reported in Cheng & Giordano 2002). From equation (2.7), it is straightfoward to see that such values correspond to a slip length of at least $\lambda_{eff}/R \approx 1/200$. As a consequence, in order to detect slip of liquids, values for the typical size R of the pipe or channel are limited to $R < 200\,\lambda_{eff}$, otherwise the change in flow rate due to slip is falling within experimental errors based on complete no-slip conditions. Since apart from the results reported by Watanabe *et al.* (1999), slip lengths for Newtonian flow in closed or open geometries have always been reported, to the best of our knowledge, to be of about 5 μm or less, this restriction on system size corresponds to the necessity to limit the size of the apparatus to approximately 1 mm. This observation allows us to understand why the influence of slip at the wall is usually not addressed or perhaps even easily measurable in studies of flow through channels or pipes of larger size.

It is worth also recognizing another possible source of error when interpreting experimental results, namely the error in the measured shear viscosity of the fluid. The value of the viscosity is extremely sensitive to the temperature; for example, near room temperature (25°C) the viscosity of water decreases approximately by 3% per degree Celsius increase in temperature. A change in temperature may have two distinct origins, an increase because of viscous heating or an increase or decrease due to a similar change in the room temperature. Let us first examine the latter; everything being equal, the dimensional flow rate in the pipe scales as the inverse of the viscosity. To fix ideas, say the temperature in a water experiment at room temperature was to increase by one degree Celsius, the shear viscosity would decrease by 3% which would lead to an increase in the flow rate of 3% approximately. From equation (2.7), we see that this increased flow rate could be misinterpreted as being due to slip at the wall with an effective dimensionless slip length $\lambda_{eff}/R \approx 0.0075$; this magnitude is, for example, of the order of what is reported in Churaev *et al.* (1984).

In addition to a change in room temperature, viscous heating of the fluid in the apparatus can contribute to a decrease in viscosity (e.g. Gavis & Laurence 1968). In the case of a steady flow, the order of magnitude of the rate of loss of mechanical energy per unit volume due to viscous effects ($\mu \dot{\gamma}^2$) is equal to the rate of change of internal energy due to conduction of temperature, $k\Delta T/R^2$; here $\dot{\gamma}$ and R are, respectively, the typical values of the shear rate and the system size, T is the temperature and k is the thermal conductivity of the fluid. Let us assume an exponential law for the dependence of the viscosity on temperature $\mu = \mu_0 \exp(-\beta(T - T_0)/T_0)$ where β is a dimensionless order one coefficient which measures the sensitivity of viscosity to variations in temperature and T_0 is a reference temperature. It is then straightforward

to obtain an order of magnitude for the relative change of viscosity due to viscous heating

$$\frac{\Delta \mu}{\mu_0} \approx \frac{\beta}{T_0} \left(\frac{\nu}{\kappa} \right) \frac{(\dot{\gamma} R)^2}{c_p}, \tag{3.1}$$

where ν is the kinematic viscosity, κ the thermal diffusivity and c_p the specific heat of the fluid. In all of the experiments summarized above, this dimensionless change of viscosity due to viscous heating varies between $\mathcal{O}(10^{-9})$ and $\mathcal{O}(10^{-3})$ which does not lead to a significant change in flow rate when compared with that measured due to effective slip and reported in table 1. Note, however, that the change in viscosity given by equation (3.1) increases as the square of the shear rate, and it is therefore possible that at higher shear than those of the experiments presented in table 1, the contribution to the increased flow rate due to viscous heating will be significant.

3.2. *Comparison of the models with experiments*

As described in §1, one physical picture for the flow over a hydrophobic (or solvophobic) surface may be that, if the surface is rough, it can support significant surface slip due to gas pockets residing along the boundary. A variant of this picture seems to hold even when the surface is nearly smooth, as evidenced by the recent observation of the presence of nano-bubbles on hydrophobic surfaces (see Ishida *et al.* 2000; Tyrrell & Attard 2001, 2002). Although the question of stability of these nano-bubbles remains an unresolved issue (e.g. Lauga & Brenner 2002) and their actual three-dimensional structure may provide additional viscous dissipation, we might envisage that such bubbles act like regions of (almost) zero shear stress along the surface, as modelled approximately by the configurations in §2. Finally, a third theoretical possibility for mixed no-slip boundaries is simply that of a surface treatment that chemically promotes slip but yet may have defects where the boundary condition is instead the usual no-slip condition.

Let us assume therefore that the experimental results from table 1 can be approximately described by the model similar to these described in figure 1 with both longitudinal and transverse no-shear patterning; we assume that the hydrophobic surfaces described in the experiments can be characterized by two sets of free dimensional parameters for the distribution of h and H describing, respectively, the typical extent of the slip regions (bubble or surface treatment) and the typical distance between them. The slip regions can be thought of as distributed somewhat randomly on the surface, both in size and orientation, and therefore the effective slip lengths obtained are presumably intermediate between those given by a distribution of transverse slip domains $\lambda_{eff,\perp}$ and those given by longitudinal slip domains $\lambda_{eff,\parallel}$. Out of the numerous degrees of freedom available for patterning of the surface, one possibility which can be addressed by the present study is the following: what is the uniform isotropic slip/no-slip patterning that would have to be considered in order to lead to the experimental results displayed in table 1? In this case, the set of unknown parameters is reduced to two unknown scalar quantities (h and H) and the effective slip length should be the same for all possible relative orientations of the slip and no-slip regions; in particular, to arrive at estimates for interpreting data, we assume $\lambda_{eff,\parallel} = \lambda_{eff,\perp}$.

With the model problems of transverse and longitudinal stripes of slip and no-slip regions, there are an infinite number of ways to distribute slip such that the resulting flow has a fixed slip length: for a given value of the dimensionless effective slip length, either in the longitudinal case ($\lambda_{eff,\parallel}/R$) or in the transverse case ($\lambda_{eff,\perp}/R$), there
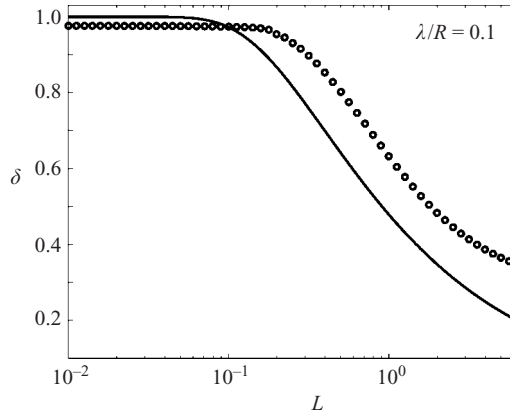
FIGURE 2. Set of coefficients of slip percentage δ and dimensionless periodicity L that lead to the same dimensionless slip length λ_{eff}/R for the transverse shear patterning model (numerical integration of (A 18), symbols) and the longitudinal no-shear patterning model (analytical formula (2.9), solid curve); the results are displayed in the case $\lambda_{eff}/R = 0.1$.

are an infinite number of slip percentages $\delta = h/R$ and dimensionless periodicities $L = H/R$ that can give such slip. This result is illustrated in figure 2 for the value $\lambda_{eff}/R = 0.1$ where the set of acceptable coefficients (L, δ) is evaluated numerically in the transverse case (symbols) and analytically in the longitudinal case (solid curve). We see, however, in figure 2 that there is only one value of the pair $(L_\lambda, \delta_\lambda)$ that results in the same value for the effective slip length in both cases, $\lambda_{eff, \parallel}(L_\lambda, \delta_\lambda) = \lambda_{eff, \perp}(L_\lambda, \delta_\lambda)$.

It is then possible to calculate numerically the set $(L_\lambda, \delta_\lambda)$ for each of the experiments described earlier; the results are displayed in the last four lines of table 1, along with the estimated sizes of the slip and no-slip regions. The obtained values for δ_λ are all within 0.5% of $\delta_\lambda = 0.97$, meaning that with this interpretation, only about 3% of the surface would be no-slip in all of the experiments; the extent of the slip regions obtained by this interpretation varies between 0.5% and 20% of the typical system size. It is worth commenting on two aspects of these results, namely the slip percentage and the size of the 'bubbles'.

First, the value $\delta_\lambda = 0.97$ is large. A possible indication of the relevance of this value may be found in Tyrrell & Attard (2001, 2002). They used atomic force microscopy to obtain images in water of nano-bubbles on smooth glass surfaces hydrophobized by dichlorodimethylsilane (angle of contact 110°). Tyrrell & Attard (2001) observe that 'the nano-bubbles do not occur in isolation with small surface coverage; they literally cover the surface, and it is difficult to see the bare substrate anywhere'; they further note in Tyrrell & Attard (2002) that 'a surprising finding is that the coverage of the surface by nano-bubbles is near 100%'. These observations indicate that the high surface coverage we obtain with our model by fitting available experimental data may not be so unreasonable. Note, however, that the distribution of the nano-bubbles in Tyrrell & Attard (2001, 2002) is qualitatively different (larger surface coverage) from those found by Ishida *et al.* (2000) on silicon wafer surfaces hydrophobized by OTS. Furthermore, the percentage of slip that we infer from our model for the experiments is much larger than the fraction of the surface that is covered with cracks in Watanabe *et al.* (1999), which is approximately 10% (see their figure 4); in this case, the possibility of connected bubbles in their system would certainly have to be considered.

Secondly, we have to consider the sizes of the slip regions obtained that are inferred with our model. Out of the five experiments, our model leads to typical bubble sizes for three of them which are in good quantitative agreement with the size of the nano-bubbles obtained by Ishida *et al.* (2000) and Tyrrell & Attard (2001, 2002) who obtained, respectively, bubbles sizes of $h = 50$–600 nm and $h = 70$ nm. In particular, for the experiments of Churaev *et al.* (1984) our model predicts $h = 34$–175 nm, for the experiment of Tretheway & Meinhart (2002) we find $h = 902$ nm, and for the experiment of Cheng & Giordano (2002) we find $h = 10$–28 nm. The experiment of Schnell (1956) leads to an estimate of bubble size $h = 2.7$–8.5 μm which is larger by almost an order of magnitude than the previous values, but we do not think this difference by itself is too significant since the slip lengths were not reported in this publication but we had to infer them from plotted pressure drop versus flow rate curves and, perhaps most importantly, details of the surface roughness in this experiment are not known. Finally, our model applied to the results of Watanabe *et al.* (1999) leads to micro-bubble sizes $h = 180$–360 μm, which far exceeds those of observed nano-bubbles, but which are consistent, however, with the pictures of elongated cracks along the surface (of size 10 μm by up to 200 μm approximately) presented in figure 4 of their article.

3.3. *Shear-dependent effective slip lengths*

At higher shear rates and if the measured slip at the wall is indeed due to surface-attached air bubbles, we argue that the effective slip length should be expected to be shear-dependent. This dependence has, however, not been clearly reported in pressure-driven flow experiments and only Churaev *et al.* (1984) briefly mentions results consistent with this idea. However, the dependence of the slip length with the fluid viscosity reported in Watanabe *et al.* (1999) and Cheng & Giordano (2002) suggests the possible importance of surface stresses.

For all of the cases displayed in table 1, the typical 'bubble' capillary number Ca defined by $Ca = \mu \dot{\gamma} h / \sigma$ can be estimated and is much smaller than unity (10^{-10} to 10^{-4}); here μ is the fluid shear viscosity, σ the gas–liquid equilibrium surface tension, h the typical size of the slip regions obtained from our model, and $\dot{\gamma}$ the shear rate at the wall. As a consequence, the bubbles would not be deformed significantly and their typical size along the flow direction is the same as their typical size across the flow. For higher shear rates, however, as soon as the capillary number reaches $\mathcal{O}(10^{-2})$ (see e.g. Taylor 1934) the bubbles will become elongated in the direction of the flow; because of this distortion, the bubble surface area will increase (at leading order the relative change in surface area is proportional to the capillary number) and therefore the percentage of the surface δ over which the fluid slips would be expected to increase. Consequently, the slip length, which is always an increasing function of δ, would increase with the shear. A shear-independent slip length can therefore be considered as the zero shear limit of a more general slip behaviour, obtained at high shear rates. A similar idea was previously proposed (based on different ideas) in the context of molecular dynamics simulations by Thompson & Troian (1997).

It is finally worth emphasizing that in squeeze flow experiments, on the contrary, strongly shear-dependent slip lengths have been reported (Craig *et al.* 2001; Zhu & Granick 2001; Bonaccurso *et al.* 2002). Such results have recently been argued to be consistent with the dynamic response to pressure fluctuations of possible gas bubbles coating the solid surfaces (Lauga & Brenner 2003).
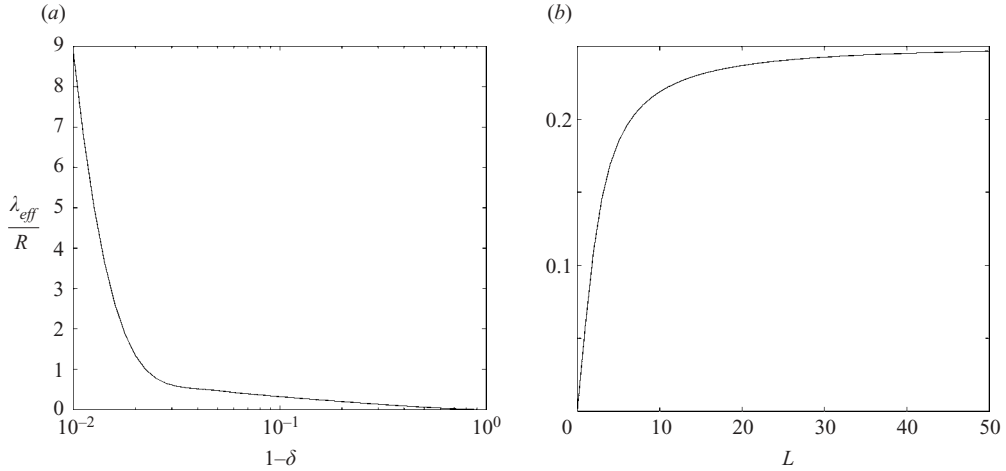
FIGURE 3. (*a*) Variation of the dimensionless slip length $\lambda_{eff,\perp}/R$ with the slip percentage δ (log scale) for $L=1$, (*b*) variation of the dimensionless slip length with the dimensionless periodicity L (log scale) for $\delta = 0.5$.

3.4. *Dependence of effective slip length on system size*

Finally, we want to comment on the increase of the slip length with system size reported by Watanabe *et al.* (1999) in their study of flow through circular pipes; note that this feature also appears to be consistent with the trends in results from different experimental groups as summarized in table 1. The results may be understood using the following argument. Let us assume that the same surface treatment is used for all the pipes used in Watanabe *et al.* (1999). The process that is responsible for the large hydrophobicity of the pipe walls is described, for simplicity, by the typical values of two scalar quantities h and H, set by the experimental method and independent of the system size; h can be thought of as the typical size of an air pocket residing along the boundary or the typical size of a slip surface treatment, and H the typical distance between them, set by the surface roughness or by the defects in the surface treatment. Increasing the system size R leads to a decrease in the dimensionless periodicity $L = H/R$, but $\delta = h/H$ remains unchanged. In the longitudinal case, and with reference to the analytical formula (2.9), we see that, for a constant δ, $\lambda_{eff,\parallel}/R$ is proportional to L, therefore $\lambda_{eff,\parallel}$ is proportional to H and does not vary with system size. In the transverse case, however, referring to the asymptotic formula (2.10*c*) for small L, and the general variation of $\lambda_{eff,\perp}/R$ with L displayed in figure 3, we see that $\lambda_{eff,\perp}/R$ is also proportional to L at the origin ($L=0$) but is concave and increases with L less rapidly than L. The variation of $\lambda_{eff,\perp}$ with respect to the system size R can be evaluated formally and is given by

$$\frac{1}{L}\frac{\mathrm{d}\lambda_{eff,\perp}}{\mathrm{d}R} = \frac{1}{L}\left(\frac{\lambda_{eff,\perp}}{R}\right) - \frac{\mathrm{d}}{\mathrm{d}L}\left(\frac{\lambda_{eff,\perp}}{R}\right). \tag{3.2}$$

Because $\lambda_{eff,\perp}/R$ is a concave function of L, it is always located below its tangent curve; as a consequence, the right-hand side of (3.2) is positive and $\mathrm{d}\lambda_{eff,\perp}/\mathrm{d}R > 0$: the dimensional transverse slip length $\lambda_{eff,\perp}$ increases with the size the system. The overall slip length λ_{eff}, which is expected to be intermediate between $\lambda_{eff,\parallel}$ and $\lambda_{eff,\perp}$ (which are not necessarily the same if the distribution is not isotropic), increases therefore with the system size.

We note that this dependence of the slip length on the system size for characterizing a macroscopic experiment illustrates an essential difference between the purely microscopic slip length (see equation (1.1)), such as those determined by molecular dynamics-like approaches, which are characteristic properties of the surfaces, and the macroscopic effective slip lengths considered here which attempt to consider the consequences of surface heterogeneities.

4. Conclusion

The possibility of slip at solid–liquid interfaces has received considerable attention in recent years, particularly now that it is common to fabricate fluid-carrying components on the micrometre and nanometre length scales. In this paper, we began by observing that small bubbles fixed at the solid boundary would act as local regions of slip embedded in an otherwise no-slip boundary. The possible existence of such bubbles has been suggested either from atomic force microscope measurements of the liquid adjacent to hydrophobic surfaces or because visual cracks are sometimes observed in the surfaces used; these cracks are even used as a design tool for super-hydropobic surfaces (Onda *et al.* 1996).

We considered two simple configurations of steady pressure-driven Stokes flow in a circular pipe with periodically distributed regions of perfect slip (infinite local slip length) and no-slip (zero local slip length), which were used to establish from pressure drop versus flow rate considerations the dependence of an effective slip length on the geometric parameters. The calculated effective slip length is to be contrasted with a molecular scale slip length which is to be applied pointwise along a solid–liquid boundary in a Navier relation (equation (1.1)).

The deduction of an effective slip length, based solely on the idea of macroscopic heterogeneities such as surface-attached bubbles, motivated a reconsideration of experimental results obtained by different groups (table 1). Several conclusions may then be drawn and several consequences are suggested: (i) in order to probe possible fluid slip at a solid boundary significantly, system sizes in the submillimetre range generally have to be considered, along with an appropriate temperature monitoring and low shear rates to avoid viscous heating; (ii) a model of uniform slip/no-slip patterning such as the one considered in this paper along with the one described in Philip (1972a) is able to reproduce sizes of slip domains consistent with the experimental observation of nano-bubbles on hydrophobic surfaces (Ishida *et al.* 2000; Tyrrell & Attard 2001, 2002) (and surface roughness in the case of Watanabe *et al.* 1999); (iii) the possibility of a shear-dependent effective slip length is suggested, based on the idea that the surface area of surface-attached bubbles, which set the amount of effective slip, depends on the wall shear stress; (iv) finally, based on the same model, we proposed an explanantion for the seemingly paradoxical increase of slip length with system size reported by Watanabe *et al.* (1999) as well as the approximate trend in table 1 for the various experiments considered.

In closing, the model presented here, and its possible extension in terms of surface-attached bubbles, neglects the three-dimensional structure of the bubbles in order to allow for simple calculations and to interpret experimental results. It is clear that this idealization underestimates the viscous dissipation, and consequently overestimates the effective slip length; however, because the typical length scales of the slip/no-slip domains are not found to be much smaller than the system size, the arguments of Richardson (1973) or Jansons (1988) predicting no-slip independently of the microscopic structure of the wall-boundary condition probably do not apply; note

also that the nano-bubbles observed by Ishida *et al.* (2000) and Tyrrell & Attard (2001, 2002) are not spherical but very flat, which reduces the influence of their geometry.

Finally, the more general issue of the stability of micro- and nano-bubbles on solid surfaces remains unclear. In particular, even though such bubbles have been observed, classical physics would predict their diffusion into the bulk almost instantaneously. Other mechanisms have therefore to be considered; in particular, both electrical effects in polar liquids and long-range intermolecular forces might play an important role in stabilizing these gas bubbles on the nanometre scale.

Appendix A. Flow in a pipe with periodic transverse distributions of slip

Let us consider the configuration shown in figure 1(*a*). The equations to solve in order to characterize the velocity field are (2.4) and (2.5). An analytical solution is obtained in §A.1. The numerical method used to solve the final set of dual series equations is described in §A.2 and typical results are given in §A.3. Finally, §A.4 presents numerical calculations and asymptotic formulae for the effective slip length as a function of the dimensionless parameters δ and L, which were introduced in §2.

A.1. *Analytical solution*

Because of the symmetries of the problem, the velocity field is axisymmetric and has a zero azimuthal component. It is therefore possible to define a streamfunction $\psi(r, z)$ by

$$u_r = \frac{1}{r}\frac{\partial \psi}{\partial z}, \quad u_z = -\frac{1}{r}\frac{\partial \psi}{\partial r}. \tag{A 1}$$

Since we are interested in the modification of the Poiseuille integral properties due to the mixed boundary conditions, a natural way to solve this linear problem is to calculate the perturbation streamfunction $\tilde{\psi}(r, t)$ to the Poiseuille flow (Ψ_p):

$$\psi(r, z) = \Psi_p(r) + \tilde{\psi}(r, z), \quad \Psi_p(r) = \tfrac{1}{16}(r^4 - 2r^2 + 1). \tag{A 2}$$

The boundary conditions for $\tilde{\psi}$ are

$$\tilde{\psi} = 0 \quad \text{for} \quad r = 1, \quad \text{all } z \tag{A 3a}$$

$$\frac{\partial \tilde{\psi}}{\partial r} = 0 \quad \text{for} \quad r = 1, \quad \tfrac{1}{2}\ell < |z| \leqslant \tfrac{1}{2}L, \tag{A 3b}$$

$$\frac{1}{2} + \frac{\partial}{\partial r}\left(\frac{1}{r}\frac{\partial \tilde{\psi}}{\partial r}\right) = 0 \quad \text{for} \quad r = 1, \quad |z| \leqslant \tfrac{1}{2}\ell. \tag{A 3c}$$

To solve for the perturbation streamfunction $\tilde{\psi}(r, z)$, we first determine the azimuthal perturbation vorticity $\tilde{\omega} = \tilde{\omega}(r, z)\mathbf{e}_\theta$, and then use the definition of the vorticity to solve for the streamfunction $\tilde{\psi}$, with the required boundary conditions (A 3a), (A 3b) and (A 3c). The equation for the perturbation vorticity is

$$\mathbf{e}_\theta \cdot \nabla^2(\tilde{\omega}(r, z)\mathbf{e}_\theta) = \left(\frac{\partial^2}{\partial z^2} + \frac{1}{r}\frac{\partial}{\partial r}\left(r\frac{\partial}{\partial r}\right) - \frac{1}{r^2}\right)\tilde{\omega} = 0. \tag{A 4}$$

The solutions to this equation can be found using separation of variables $\tilde{\omega}(r, z) = f_n(r) \cos(k_n z)$, with $k_n = 2n\pi/L$, $n = 0, 1, 2, \ldots$ required by periodicity and f_n satisfying a modified Bessel equation of order 1,

$$r^2 f_n'' + r f_n' - (1 + k_n^2 r^2) f_n = 0, \quad \text{so} \quad f_0(r) = a_0 r, \quad f_n(r) = a_n I_1(k_n r) + b_n K_1(k_n r), \quad n \geqslant 1. \tag{A 5}$$

Here, I_i and K_i are, respectively, the modified Bessel functions of the first and second kind of order i. Because the vorticity must be bounded at the origin $r = 0$, we take $b_n = 0$ and therefore the vorticity is expressed as a Bessel–Fourier series

$$\tilde{\omega}(r, z) = \frac{\partial \tilde{u}_r}{\partial z} - \frac{\partial \tilde{u}_z}{\partial r} = a_0 r + \sum_{n=1}^{\infty} a_n I_1(k_n r) \cos(k_n z). \tag{A 6}$$

The definition of the vorticity in terms of the streamfunction is

$$\tilde{\omega}(r, z) = \left(\frac{1}{r} \frac{\partial^2}{\partial z^2} + \frac{\partial}{\partial r} \left(\frac{1}{r} \frac{\partial}{\partial r} \right) \right) \tilde{\psi}. \tag{A 7}$$

The streamfunction can therefore be expressed using the same separation of variables as the vorticity with the result

$$\tilde{\psi}(r, z) = \tfrac{1}{8} a_0 r^4 + c_0 r^2 + d_0 + \sum_{n=1}^{\infty} \frac{a_n}{k_n^3} g_n(k_n r) \cos(k_n z). \tag{A 8}$$

By substituting equation (A 8) into (A 7), we find that the $g_n(x)$ are equal to the same function $g(x)$, which satisfies the ordinary differential equation

$$x^2 g'' - x g' - x^2 g = x^3 I_1(x). \tag{A 9}$$

The general solution to equation (A 9) is $g(x) = C_2 x I_1(x) + C_3 x K_1(x) + x H(x)$ where $H(x)$ is given by

$$H(x) = I_1(x) \int_0^x t K_1(t) I_1(t) \, \mathrm{d}t + \tfrac{1}{2} x^2 K_1(x) (I_0(x) I_2(x) - I_1(x)^2). \tag{A 10}$$

Because the streamwise component of the velocity u_z must be bounded, we need $x^{-1} g'(x)$ bounded everywhere inside the pipe which leads to $C_3 = 0$, and the general solution for the perturbation streamfunction is therefore given by

$$\tilde{\psi}(r, z) = \tfrac{1}{8} a_0 r^4 + c_0 r^2 + d_0 + \sum_{n=1}^{\infty} k_n r \left[\frac{a_n}{k_n^3} H(k_n r) + c_n I_1(k_n r) \right] \cos(k_n z). \tag{A 11}$$

Moreover, since $\tilde{\psi}$ is the perturbation streamfunction, it results in a zero mean pressure gradient, and therefore $a_0 = 0$. The remaining set of unknown constants $(c_0, d_0, \{a_n\}, \{c_n\})$ has to be determined using the mixed boundary conditions (A 3a), (A 3b) and (A 3c). Applying the boundary condition (A 3a) leads to $c_0 + d_0 = 0$ and $c_n I_1(k_n) + a_n H(k_n)/k_n^3 = 0$ and therefore to the general form of the streamfunction

$$\tilde{\psi}(r, z) = \alpha_0 (1 - r^2) + \sum_{n=1}^{\infty} \alpha_n k_n r \left[I_1(k_n) H(k_n r) - H(k_n) I_1(k_n r) \right] \cos(k_n z), \tag{A 12}$$

where we have simply relabelled coefficients $\alpha_n = a_n/(k_n^3 I_1(k_n))$ and $\alpha_0 = c_0$. The set of coefficients $\{\alpha_n\}$ remains to be determined. They cannot be inferred from any other condition inside the pipe; therefore the coefficients will be determined by the

boundary conditions (A 3b) and (A 3c), and will depend on both the values of ℓ and L. Boundary condition (A 3b) on the no-slip portion of the domain and (A 3c) on the no-shear portion of the domain lead to dual series equations for the coefficients $\{\alpha_n\}$,

$$-\alpha_0 + \sum_{n=1}^{\infty} \alpha_n R(k_n) \cos(k_n z) = 0 \quad \text{for} \quad \tfrac{1}{2}\ell < |z| \leqslant \tfrac{1}{2}L, \tag{A 13a}$$

$$\tfrac{1}{16} + \sum_{n=1}^{\infty} \alpha_n S(k_n) \cos(k_n z) = 0 \quad \text{for} \quad |z| \leqslant \tfrac{1}{2}\ell, \tag{A 13b}$$

where the functions $R(x)$ and $S(x)$ are given by

$$R(x) = \tfrac{1}{4}x^3 \left(I_1^2(x) - I_0^2(x)\right) + \tfrac{1}{2}x^2 I_0(x) I_1(x), \quad S(x) = \tfrac{1}{8}x^3 I_1^2(x). \tag{A 14}$$

Note that the identity $K_0(x)I_1(x) + K_1(x)I_0(x) = 1/x$ was used to obtain (A 14). The dual series equations (A 13a)–(A 13b) do not have a standard form (see Sneddon 1966) and therefore have to be solved numerically for each value of ℓ and L. After the set of coefficients $\{\alpha_n\}$ is determined, the dimensionless velocity field can be evaluated and is given by

$$u_r(r, z) = -\sum_{n=1}^{\infty} \alpha_n k_n^2 \left[I_1(k_n)H(k_n r) - H(k_n)I_1(k_n r)\right] \sin(k_n z) \tag{A 15}$$

and

$$u_z(r, z) = \tfrac{1}{4}(1 - r^2) + 2\alpha_0 - \sum_{n=1}^{\infty} \alpha_n k_n^2 \left[I_1(k_n)M(k_n r) - H(k_n)I_0(k_n r)\right] \cos(k_n z), \tag{A 16}$$

with

$$M(x) = I_0(x) \int_0^x t K_1(t) I_1(t) \, \mathrm{d}t + \tfrac{1}{2}x^2 K_0(x)(I_1(x)^2 - I_0(x)I_2(x)). \tag{A 17}$$

A.2. *Numerical integration of the dual series equations*

In order to solve equations (A 13) it is convenient to make the change of variable $x = z/L$ and define $\delta = \ell/L = h/H$; δ is therefore the total fraction of the surface that is perfect slip and we have $0 \leqslant \delta \leqslant 1$. The dual series equations become

$$-\alpha_0 + \sum_{n=1}^{\infty} \alpha_n R(k_n) \cos(2n\pi x) = 0 \quad \text{for} \quad \tfrac{1}{2}\delta < |x| \leqslant \tfrac{1}{2}, \tag{A 18a}$$

$$\tfrac{1}{16} + \sum_{n=1}^{\infty} \alpha_n S(k_n) \cos(2n\pi x) = 0 \quad \text{for} \quad |x| \leqslant \tfrac{1}{2}\delta. \tag{A 18b}$$

The solution depends therefore not only on δ, but also on how this slip is distributed (a different number of rings for a given slip percentage, i.e. different values of L for a given δ). To solve this equation for $\{\alpha_n\}$ numerically, we truncate the dual series equation at α_{N-1} and calculate its inner product on the interval $x \in [0, 1/2]$ with $\cos(2m\pi x)$, with $m \in [0, N-1]$. We then obtain a linear system of equations for the α_n coefficients. However, as written in equation (A 18), the system is not well suited to a numerical integration because both the functions R and S diverge rapidly to $+\infty$ when n becomes large. However, the asymptotic behaviours of Bessel functions for large arguments are known and we can use them to rescale the dual series equations and

look for new well conditioned unknowns. Near $x \sim +\infty$, we have (see Abramowitz & Stegun 1972)

$$I_\nu(x) \sim \frac{e^x}{\sqrt{2\pi x}} \left\{ 1 - \frac{4\nu^2 - 1}{8x} \right\}, \tag{A 19}$$

so it is therefore straightforward to obtain

$$R(x) \sim \frac{xe^{2x}}{8\pi} \left\{ 1 - \frac{3}{8x} \right\}, \quad S(x) \sim \frac{x^2 e^{2x}}{16\pi} \left\{ 1 - \frac{3}{4x} \right\} \quad (x \to +\infty). \tag{A 20}$$

The dual series equation is then solved by dividing $R(k_n)$ and $S(k_n)$ by the asymptotic behaviour $xe^{2x}/8\pi$ and therefore modifying the definitions of α_n for $n \geqslant 1$. The resulting system is then found to be well conditioned and calculations are found to converge upon truncation refinement.

A.3. *Calculation of the slip length*

In the case studied here, the additional flow rate $\tilde{Q} = Q - \pi/8$, independent of z by mass conservation, can be calculated using the definitions of the streamfunction (A 1) and (A 12) and the definition of the slip length (2.8), and we obtain

$$\tilde{Q} = 2\pi \int_0^1 r\tilde{u}_z(r, z)\, dr = 2\pi\tilde{\psi}(0) = 2\pi\alpha_0 \quad \text{and therefore} \quad \frac{\lambda_{eff, \perp}}{R} = 4\alpha_0. \tag{A 21}$$

With the numerical procedure described in § A.2, the slip length was found to converge quickly to a final value upon increasing the truncation number of the dual series equations.

A typical calculation for the dimensionless slip length $\lambda_{eff, \perp}/R$ is depicted in figure 3(*a*) as a function of the no-slip percentage $1 - \delta$, for the case $L = 1$. When the slip percentage $\delta \to 0$, the slip length decreases to zero and the flow profile tends to the Poiseuille profile. When δ increases, the slip length increases also as expected and when $\delta \to 1$, the slip length diverges to $+\infty$ as the flow tends to a plug flow profile. A similar calculation for the dimensionless slip length $\lambda_{eff, \perp}/R$ as a function of the dimensionless period L is displayed in figure 3(*b*), for the case $\delta = 0.5$. When $L \to 0$, the slip length goes to zero, which is also the case for a pressure-driven pipe flow with longitudinal regions of slip and no-slip (see Philip 1972*b* and § 3). When L increases, the slip length increases and tends to an asymptotic value when $L \to +\infty$, which depends only on the slip percentage δ, as derived in the next section.

A.4. *Asymptotic behaviours for the dimensionless slip length*

We determine in this section the asymptotic behaviours for the slip length as a function of δ and L in four different regions of the parameter space: small and large amounts of slip δ and small and large distances between the slip regions L. In all cases, the obtained asymptotic behaviours are found to agree with numerical calculations.

A.4.1. *Limit of small amount of slip*

Let us first calculate the asymptotic behaviour for the dimensionless slip length in the case where the distance between the rings is fixed and the percentage of the surface which is slip δ goes to zero. In this case, the flow tends to the Poiseuille flow profile and the slip length decreases to zero. The mean value of the entire dual series

equations (A 18a, b) leads to the equality

$$\delta \sum_{n=1}^{\infty} \alpha_n (S(k_n) - R(k_n)) \, W(n\pi\delta) = \alpha_0 - \delta\left(\alpha_0 + \tfrac{1}{16}\right), \qquad (A\,22)$$

where $W(x) = \sin(x)/x$. Since in the limit $\delta \to 0$, the left-hand side of equation (A 18b) becomes an exact Fourier series for the function 0, each of the coefficients $\{\alpha_n\}$ is zero in this limit. The function $W(x)$ being bounded by 1 and the set of coefficients $R(k_n)$ and $S(k_n)$ not depending on δ, we therefore obtain when $\delta \to 0$ that the left-hand side of equation (A 22) is much smaller than δ; the order $O(\delta)$ of the right-hand side of equation (A 22) has therefore to vanish, which leads to the asymptotic behaviour $\alpha_0 \sim \delta/16$, and so by (A 21), we obtain a linear asymptotic behaviour for the slip length

$$\frac{\lambda_{eff,\perp}}{R} \sim \frac{\delta}{4} \quad (\lim \delta \to 0). \qquad (A\,23)$$

As expected, the slip length decreases to zero in the limit of vanishing perfect slip regions; furthermore, its asymptotic behaviour depends on the distance $L = H/R$ between the slip regions only through $\delta = \ell/L$. A numerical validation of the dependence (A 23) for the slip length as a function of the slip percentage δ is provided in figure 4(a) for $L = 0.01$ and 1. The results are displayed on a log–log scale and confirm the theoretical linear dependence of λ_{eff}/R with δ.

A.4.2. *Limit of large amount of slip*

We next calculate the asymptotic behaviour for $\lambda_{eff,\perp}/R$ in the case where the distance between the rings is fixed and the percentage of the surface on which the fluid slips goes to 100 %, i.e. $\delta \to 1$. In this case, the tube offers almost no resistance to the fluid, and therefore the flow tends to a plug flow profile corresponding to $\lambda_{eff} \to +\infty$. Equation (A 22) can now be rewritten as

$$\sum_{n=1}^{\infty} \alpha_n (S(k_n) - R(k_n)) \left[\frac{\sin(n\pi\delta)}{n\pi} \right] = \alpha_0(1 - \delta) - \frac{\delta}{16}. \qquad (A\,24)$$

Moreover, when evaluating equation (A 18b) for $x = 0$, we obtain $\sum \alpha_n S(k_n) + 1/16 = 0$, which is valid for all values of δ, and therefore valid also for the limit $\delta \to 1$. Since the function $S(x)$ is never equal to zero, the coefficients α_n are therefore always bounded for $n \geqslant 1$. Moreover, when $\delta \to 1$, $\sin(n\pi\delta) \to 0$. Consequently, when taking the limit $\delta \to 1$ with L fixed, the left-hand side of equation (A 24) goes to zero. The $O(1)$ limit of the right-hand side of (A 24) has therefore to be zero, which leads to $(1 - \delta)\alpha_0 \sim 1/16$, and corresponds to the asymptotic behaviour for the slip length

$$\frac{\lambda_{eff,\perp}}{R} \sim \frac{1}{4(1 - \delta)} \quad (\lim \delta \to 1). \qquad (A\,25)$$

As expected, the slip length increases to $+\infty$ in the limit of a large amount of slip and, again, its asymptotic behaviour depends on the periodicity L only through $\delta = \ell/L$. The obtained variation (A 25) of the slip length as a function of the no-slip percentage $(1 - \delta)$ is confirmed numerically in figure 4(b) for $L = 0.01$ and 1.

A.4.3. *Limit of small distance between slip regions*

Let us now calculate the asymptotic behaviour for the dimensionless slip length in the case where the slip percentage is fixed, but the distance between the rings
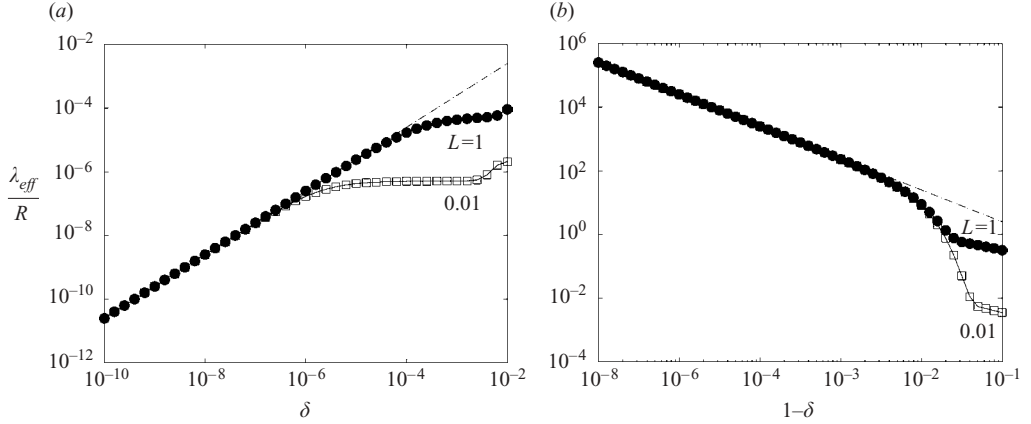
FIGURE 4. Asymptotic behaviours for the dimensionless slip length $\lambda_{eff,\perp}/R$ for fixed L. (a) Limit of no-slip $\delta \to 0$ calculated numerically (symbols, log–log scale) with the theoretical prediction (A 23) (dashed); (b) limit of perfect slip $\delta \to 1$ calculated numerically (symbols) with the theoretical prediction (A 25) (dashed). In each case, the results are reported for $L = 0.01$ (squares) and $L = 1$ (circles).

goes to zero. Using the asymptotic forms (A 20) for the functions R and S and the set of coefficients $\{\alpha_n\}$ rescaled as proposed in §A.2, it is clear that when $L \to 0$ then $k_n \to +\infty$ and therefore $R(k_n)$ and $S(k_n)$ can be replaced in the dual series equations (A 18a) and (A 18b) by their asymptotic behaviours $R(k_n) \sim 1$ and $S(k_n) \sim k_n/2$. After performing the change of variable $y = 2\pi x$ in (A 18a) and (A 18b), the dual series equation can then be rewritten in a standard form (see Sneddon 1966)

$$-\alpha_0 + \sum_{n=1}^{\infty} \alpha_n \cos(ny) = 0 \quad \text{for} \quad \delta\pi < y \leqslant \pi, \qquad (A\,26a)$$

$$\frac{L}{16\pi} + \sum_{n=1}^{\infty} n\,\alpha_n \cos(ny) = 0 \quad \text{for} \quad y \leqslant \delta\pi. \qquad (A\,26b)$$

The new dual series equations (A 26) can be solved exactly (see Sneddon 1966) to obtain

$$\frac{\lambda_{eff,\perp}}{R} \sim \frac{L}{2\pi} \ln\left(\sec\left(\delta\frac{\pi}{2}\right)\right) \quad (\lim L \to 0). \qquad (A\,27)$$

For a given slip percentage, the slip length $\lambda_{eff,\perp}$ decreases to zero as the periodicity $L \to 0$, which confirms the general trend from figure 3(c). Note also that two different expressions are obtained for the two asymptotic limits (1) L fixed, $\delta \to 0$ (equation (A 23)) and (2) δ fixed, $L \to 0$ (equation (A 27)). A numerical confirmation of equation (A 27) for the slip length as a function of the periodicity L is provided in figure (5a) for $\delta = 0.2$. The results are displayed on a log–log scale and show both the linear dependence of $\lambda_{eff,\perp}/R$ with L and the theoretical dependence of the asymptotic behaviour with the slip percentage δ (i.e. the slope of the curve in figure 5a).

A.4.4. *Limit of large distance between slip regions*

Finally, let us consider the case where the amount of slip δ is fixed, but the distance between the rings diverges to $+\infty$. To derive the result for this asymptotic limit we need to evaluate $R(k_n)$ and $S(k_n)$ when the argument $k_n = 2\pi n/L \to 0$. The asymptotic
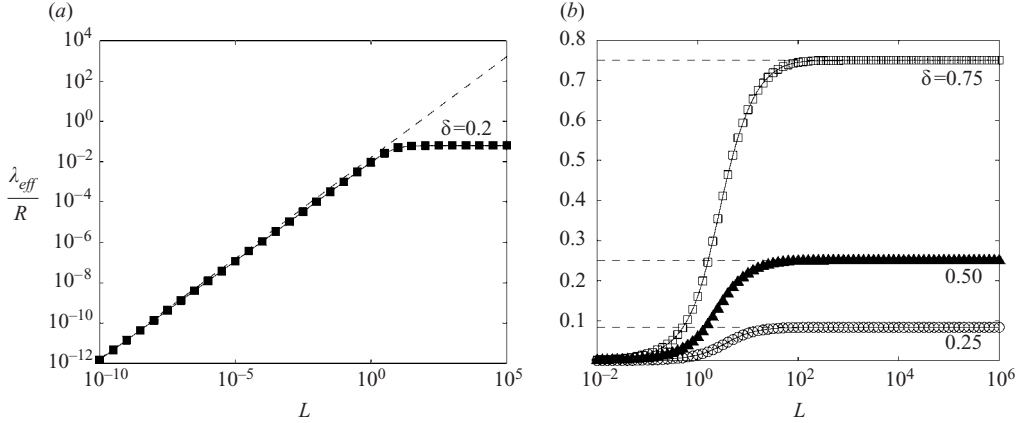
FIGURE 5. Asymptotic behaviours for the dimensionless slip length $\lambda_{eff,\perp}/R$ when δ is fixed. (a) Limit of small periodicity $L \to 0$ calculated numerically (squares, log–log scale) with the theoretical prediction (A 27) (dashed) for $\delta = 0.2$. (b) Limit of large periodicity $L \to +\infty$ calculated numerically (symbols, log–log scale) with the theoretical predictions (A 29) (dashed), for $\delta = 0.25$ (circles), 0.5 (triangles) and 0.75 (squares).

behaviour of the modified Bessel function near the origin is (see Abramowitz & Stegun 1972)

$$I_v(x) \sim \frac{\left(\frac{1}{2}x\right)^v}{\Gamma(1+v)} \left\{ 1 + \frac{\Gamma(1+v)}{\Gamma(2+v)} \frac{x^2}{4} + O(x^4) \right\}, \qquad (A\,28)$$

and therefore, when $x \to 0^+$, the functions R and S have the same asymptotic behaviour $R(x) \sim S(x) \sim x^5/32$. Hence, the coefficients $R(k_n)$ and $S(k_n)$ in the dual series equations (A 18a) and (A 18b) have the same behaviour as $L \to +\infty$. Since we can always rescale the set of unknown coefficients $\{\alpha_n\}$ by the asymptotic behaviour above, we can replace, without loss of generality, $R(k_n)$ and $S(k_n)$ by 1 in the limit of large L. Taking the mean value of the obtained dual series equation leads to the asymptotic behaviour for the dimensionless slip length

$$\frac{\lambda_{eff,\perp}}{R} = \frac{\delta}{4(1-\delta)} \quad (\lim L \to +\infty). \qquad (A\,29)$$

As a consequence, when the separation between the slip regions becomes large but the amount of slip is fixed, the dimensionless slip length tends to an asymptotic constant which is independent of L. In the limit where $\delta \to 0$ and $\delta \to 1$, the results of §A.4.1 and A.4.2 are recovered. The theoretical prediction for the asympotic limit (A 29) of the slip length obtained above is confirmed numerically in figure 5(b) for $\delta = 0.25$, 0.5 and 0.75.

Appendix B. Flow in a pipe with periodic longitudinal distributions of slip, by Philip (1972a, b)

We now consider the case where the no-slip domains are distributed in a longitudinal fashion, such as illustrated in figure 1(b). The solution is derived in Philip (1972a) and we recall it here. Consider the Poiseuille flow in the z-direction in a pipe of radius R modified by the presence of m equally spaced longitudinal no-shear bands, each of

half-angle α. The velocity in the pipe is given by

$$u_z(r, \theta) = -\frac{R^2}{4\mu} \frac{\mathrm{d}p}{\mathrm{d}z} \left\{ 1 - \left(\frac{r}{R} \right)^2 + \frac{4}{m} \mathrm{Im} \left\{ \cos^{-1} \left(\frac{\cos(\Lambda)}{\cos(m\alpha/2)} \right) - \Lambda \right\} \right\} \qquad (B\,1)$$

with

$$\Lambda = -\tfrac{1}{2}\mathrm{i}m \ln \left(\frac{r\mathrm{e}^{\mathrm{i}\theta}}{R} \right), \qquad (B\,2)$$

and where Im denotes the imaginary part of the function. In this case, the effective slip length $\lambda_{eff,\,\|}$ can be calculated exactly from the pressure drop versus flow rates formulae given in Philip (1972b) and is given by

$$\frac{\lambda_{eff,\,\|}}{R} = \frac{2}{m} \ln \left(\sec \left(\frac{m\alpha}{2} \right) \right). \qquad (B\,3)$$

Other calculations are offered in Philip (1972a) for different geometrical configurations and distribution of slip and no-slip regions. We have also tabulated these solutions using notations consistent with the rest of the present paper and the interested reader can contact the authors.

REFERENCES

ABRAMOWITZ, M. & STEGUN, I. A. 1972 *Handbook of Mathematical Functions*. Dover.

BARRAT, J.-L. & BOCQUET, L. 1999 Large slip effect at a nonwetting fluid–solid interface. *Phys. Rev. Lett.* **82**, 4671–4674.

BAUDRY, J. & CHARLAIX, E. 2001 Experimental evidence for a large slip effect at a nonwetting fluid–solid interface. *Langmuir* **17**, 5232–5236.

BEAN, C. P. 1972 The physics of porous membranes. *Membranes* 1 (ed. G. Eisenman). Marcel Dekker.

BOEHNKE, U.-C., REMMLER, T., MOTSCHMANN, M., WURLITZER, S., HAUWEDE, J. & FISHER, TH. M. 1999 Partial air wetting on solvophobic surfaces in polar liquids. *J. Colloid. Interface Sci.* **211**, 243–251.

BONACCURSO, E., KAPPL, M. & BUTT, H.-S. 2002 Hydrodynamic force measurements: boundary slip of water on hydrophilic surfaces and electrokinetic effects. *Phys. Rev. Lett.* **88**, 076103.

BRENNER, H. & GANESAN, V. 2000 Molecular wall effects: are conditions at a boundary 'boundary conditions'? *Phys. Rev. E* **61**, 6879–6897.

CHAN, D. Y. C. & HORN, R. G. 1985 The drainage of thin liquids films between solid surfaces. *J. Chem. Phys.* **83**, 5311–5324.

CHENG, J.-T. & GIORDANO, N. 2002 Fluid flow through nanometre-scale channels. *Phys. Rev. E* **65**, 031206.

CHURAEV, N. V., SOBOLEV, V. D. & SOMOV, A. N. 1984 Slippage of liquids over lyophobic solid surfaces. *J. Colloid. Interface Sci.* **97**, 574–581.

CIEPLAK, M., KOPLIK, J. & BANAVAR, J. R. 2001 Boundary conditions at a fluid–solid interface. *Phys. Rev. Lett.* **86**, 803–806.

COTTIN-BIZONNE, C., JURINE, S., BAUDRY, J., CRASSOUS, J., RESTAGNO, F. & CHARLAIX, É. 2002 Nanorheology: an investigation of the boundary condition at hydrophobic and hydrophilic interfaces. *Eur. Phys. J. E* **9**, 47–53.

CRAIG, V. S. J., NETO, C. & WILLIAMS, D. R. M. 2001 Shear-dependent boundary slip in an aqueous Newtonian liquid. *Phys. Rev. Lett.* **87**, 054504.

DENNISTON, C. & ROBBINS, M. O. 2001 Molecular and continuum boundary conditions for a miscible binary fluid. *Phys. Rev. Lett.* **87**, 178302.

GANESAN, V. & BRENNER, H. 1999 Comment on 'no-slip condition for a mixture of two liquids'. *Phys. Rev. Lett.* **82**, 1333.

GAVIS, J. & LAURENCE, R. L. 1968 Viscous heating in plane and circular flow between moving surfaces. *I&EC Fundamentals* **7**, 232–239.

IDOL, W. K. & ANDERSON, J. L. 1986 Effects of adsorbed polyelectrolytes on convective flow and diffusion in porous membranes. *J. Memb. Sci.* **28**, 269–286.

ISHIDA, N., INOUE, T., MIYAHARA, M. & HIGASHITANI, K. 2000 Nano bubbles on a hydrophobic surface in water observed by tapping-mode atomic force microscopy. *Langmuir* **16**, 6377–6380.

JANSONS, K. M. 1988 Determination of the macroscopic (partial) slip boundary condition for a viscous flow over a randomly rough surface with a perfect slip microscopic boundary condition. *Phys. Fluids* **31**, 15–17.

KNUDSTRUP, T. G., BITSANIS, I. A. & WESTERMANN-CLARK, G. B. 1995 Pressure-driven flow experiments in molecularly narrow, straight pores of molecular dimension in mica. *Langmuir* **11**, 893–897.

KOPLIK, J. & BANAVAR, J. R. 1995 Continuum deductions from molecular hydrodynamics. *Annu. Rev. Fluid Mech.* **27**, 257–292.

KOPLIK, J. & BANAVAR, J. R. 1999 Reply to comment on 'No-slip condition for a mixture of two liquids'. *Phys. Rev. Lett.* **82**, 1334.

LAUGA, E. & BRENNER, M. P. 2003 Dynamic mechanisms for apparent slip on hydrophobic surfaces. *Euro. Phys. Lett.* (submitted).

MAXWELL, J. C. 1879 On stresses in rarified gases arising from inequalities of temperature. *Phil. Trans. R. Soc. Lond.* **170**, 231–256.

NAVIER, C. L. M. H. 1823 Mémoire sur les lois du mouvement des fluides. *Mémoires de l'Académie Royale des Sciences de l'Institut de France* **6**, 389–440.

ONDA, T., SHIBUICHI, S., SATOH, N. & TSUJI, K. 1996 Super-water-repellent fractal surfaces. *Langmuir* **12**, 2125–2127.

PHILIP, J. R. 1972a Flows satisfying mixed no-slip and no-shear conditions. *Z. Angew. Math. Phys.* **23**, 353–370.

PHILIP, J. R. 1972b Integral properties of flows satisfying mixed no-slip and no-shear conditions. *Z. Angew. Math. Phys.* **23**, 960–968.

PIT, R., HERVERT, H. & LÉGER, L. 2000 Direct experimental evidence of slip in hexadecane: solid interfaces. *Phys. Rev. Lett.* **85**, 980–983.

QUINN, J. A., ANDERSON, J. L., HO, W. S. & PETZNY, W. J. 1972 Model pores of molecular dimension: the preparation and characterization of track-etched membranes. *Biophys. J.* **12**, 990–1007.

RAVIV, U., GIASSON, S., FREY, J. & KLEIN, J. 2002 Viscosity of ultra thin water films confined between hydrophobic or hydrophilic surfaces. *J. Phys.: Condens. Matter* **14**, 9275–9283.

RICHARDSON, S. 1973 On the no-slip boundary condition. *J. Fluid Mech.* **59**, 707–719.

ROBBINS, M. O. 1990 Shear flow near solids: epitaxial order and flow boundary conditions. *Phys. Rev. A* **41**, 6830–6837.

SCHNELL, E. 1956 Slippage of water over nonwettable surfaces. *J. Appl. Phys.* **27**, 1149–1152.

SNEDDON, I. N. 1966 *Mixed Boundary Value Problems in Potential Theory*. North-Holland.

TAYLOR, G. I. 1934 The formation of emulsions in definable fields of flow. *Proc. R. Soc. A* **146**, 501–523.

THOMPSON, P. A. & TROIAN, S. M. 1997 A general boundary condition for liquid flow at solid surfaces. *Nature* **389**, 360–362.

TRETHEWAY, D. C. & MEINHART, C. D. 2002 Apparent fluid slip at hydrophobic microchannel walls. *Phys. Fluids* **14**, L9–L12.

TYRRELL, J. W. G. & ATTARD, P. 2001 Images of nanobubbles on hydrophobic surfaces and their interactions. *Phys. Rev. Lett.* **87**, 176104.

TYRRELL, J. W. G. & ATTARD, P. 2002 Atomic force microscope images of nanobubbles on a hydrophobic surface and corresponding force-separation data. *Langmuir* **18**, 160–167.

VINOGRADOVA, O. I. 1999 Slippage of water over hydrophobic surfaces. *Intl J. Miner. Process.* **56**, 31–60.

WATANABE, K., UDAGAWA, Y. & UDAGAWA, H. 1999 Drag reduction of Newtonian fluid in a circular pipe with a highly water-repellent wall. *J. Fluid Mech.* **381**, 225–238.

ZHU, Y. & GRANICK, S. 2001 Rate-dependent slip of Newtonian liquid at smooth surfaces. *Phys. Rev. Lett.* **87**, 096105.

ZHU, Y. & GRANICK, S. 2002 On the origin of the no-slip boundary condition. *Phys. Rev. Lett.* **88**, 106102.